Superlattices and Microstructures 125 (2019) 16–25

Contents lists available at ScienceDirect

Superlattices and Microstructures

journal homepage: www.elsevier.com/locate/superlattices

The investigation of [Fe/Cr] multilayer by GISAXS

A.V. Ragulskaya[a], M.A. Andreeva[a,*], A.V. Rogachev[b], S.N. Yakunin[b]

[a] Faculty of Physics, Lomonosov Moscow State University, Moscow, 119991 Russia
[b] National Research Center Kurchatov Institute, Moscow, 123182 Russia

ARTICLE INFO

Keywords:
X-ray scattering
Grazing incidence
X-ray reflectivity
Distorted wave born approximation (DWBA)
Cluster-layered multilayers
X-ray standing waves

ABSTRACT

Grazing Incidence Small Angle X-ray Scattering (GISAXS) has been used for characterization of a cluster structure of the $[Fe/Cr]_{30}$ multilayer with ultrathin iron layers. The experiment was performed at the "Langmuir" station of the Kurchatov Center of Synchrotron Radiation and Nanotechnology. Experimental GISAXS image has shown the side satellites and the Bragg peak revealing the existence of density inhomogeneities with an average lateral distance of ∼19 nm periodically repeated along depth. The modelling of the obtained image has been done in the DWBA approximation. It has been shown that for the wavelength used in the experiment (0.0951 nm) it is not possible to distinguish if the inhomogeneities exist in the Fe or in the Cr layers due to the small optical contrast between Fe and Cr layers. However, as it has been demonstrated by model calculations, in the case of the enhanced optical contrast (e.g. for the wavelength corresponding to the L_3 edge of Fe) the x-ray standing waves allow ones to select the cases of inhomogeneities in the Fe or in the Cr layers: the simulated GISAXS patterns are rather different for these two cases.

1. Introduction

The unique properties of ultrathin metal films have created an entirely new field of magnetism which already has a profound impact in the development of magnetic devices for information technology and for applications in areas such as magnetic sensors, recording materials, and novel devices such as spin filters or transistors [1,2]. Cluster-layered multilayer structures [Fe/Cr] with ultrathin layers of ferromagnetic constituent show a big variety of interesting magnetic properties such as giant magnetoresistance (GMR), Kondo-like behavior etc. [3,4]. These properties strongly depend on layer thicknesses and its continuity, layer structure, quality of the interfaces. Knowledge of the relations between morphology and physical properties of nanometer-scaled objects is key to engineer the functionalities of devices in nanotechnology. The structure analysis of such multilayers becomes more and more important in the last years due to the strongly increasing field of nanotechnology and surface science. The common methods for its characterization: the high angle X-ray diffraction and low angle X-ray reflectivity, atomic force microscopy, polarized neutron reflectivity do not give the buried layer morphology and features of the internal local structure. The sample can show quite nice reflectivity curve with several Bragg maxima confirming the good periodicity of the layer structure, but these data characterize only the average periodicity along the surface.

Such result has been obtained for the $[Fe/Cr]_n$ multilayers with ultrathin ^{57}Fe layers, prepared by magnetron sputtering in IFM RAN (Ekaterinburg, Russia). The measured reflectivity curves were quite good with Bragg peaks and Kiessih oscillations, however, the measurements of the angular distribution of the reflected radiation give a rather broad angular spectra (∼200″), characterizing

* Corresponding author.
E-mail address: Mandreeva1@yandex.ru (M.A. Andreeva).

https://doi.org/10.1016/j.spmi.2018.10.017
Received 29 August 2018; Accepted 16 October 2018
Available online 17 October 2018

complicated lateral relief of the surface and probably density inhomogeneities in the internal layers [5,6].

Grazing-incidence small-angle X-ray scattering (GISAXS) is a novel technique developed for characterizing nanoobjects at the surface or lateral variations of the electron density inside the sample (see review [7] and basic theory in Ref. [8]). The most developed applications of GISAXS refer to characterizing the self-assembly and self-organization on the nanoobjects on the surface of strongly reflected substrate or in thin films [9–16]. The high intensity of the synchrotron sources gives the possibility to perform such measurements as a function of time with very high temporal resolution and down to microsecond timescales. The interesting effects induced by neon and helium implantation have been observed in silicon by GISAXS measurements [17]. Buried nanostructures have been investigated by GISAXS with the application of the X-ray standing wave technique [18]. The combination of GISAXS and nuclear resonant reflectivity gives the information about the magnetic ordering of different structural units of a nanostructured sample separately [19]. The inner structure of multilayers has been examined by GISAXS only in a few papers [20–24].

In these article the results of GISAXS measurements are presented for Al_2O_3/Cr(70 Å)/[^{57}Fe(8 Å)/Cr(10.5 Å)]$_{30}$/Cr(12 Å) sample (the nominal thicknesses are indicated). For the interpretation of these results the simplified theory has been used and model calculations reproduce the basic features of the experimental pattern for a proper depth profile of inhomogeneities. The question has been examined how to select the source layers for the side maxima on the GISAXS image and is has been shown that the combination of the GISAXS measurements with the X-ray standing wave method supply us with information about depth profiling of the inhomogeneities.

2. Experiment

The measurements have been done at the "Langmuir" station of the Kurchatov Center of Synchrotron Radiation and Nanotechnology. GISAXS image has been obtained with monochromatated radiation (0.0951 nm wavelength) at the grazing incidence angle $\theta_i = 8.37$ mrad (Fig. 1). The chosen angle is more than twice larger than the critical angle of the total external reflection ($\sim$4.19 mrad) and at this angle the radiation penetrates through the whole structure. Therefore the obtained GISAXS picture contains information not only from the very surface layers but from deeper layers as well. The angle θ_f is the angle of the scattered radiation with the surface plane, the angle ψ is the angle of the deviation of the scattered radiation from the reflection plane.

The cross sections of the image presented Fig. 1(b) are obtained with DPDAK program package [25]. The Bragg peak at $\theta_f \approx 51.46$ mrad on the obtained picture is an evidence of the periodicity along depth for the inhomogeneity distribution. The side maxima at $\psi \approx \pm 5$ mrad characterize some correlations in a lateral distribution of density inhomogeneities. The simple Bragg law for these maxima gives the period of the structure D and average lateral distance between inhomogeneities d_{corr}.

$$D \approx \frac{\lambda}{2\sin\left(\frac{\theta_i+\theta_f}{2}\right)} \approx 1.6\ \text{nm},\ d_{corr} \approx \frac{\lambda}{2\sin(\psi/2)} \approx 19.1\ \text{nm}. \tag{1}$$

These estimations are confirmed by more accurate model calculations. In Fig. 1(b) it is seen that the scattered intensity near the Bragg peak is broader along ψ than that one near the critical angle, it can be supposed that the average lateral size of the density inhomogeneities is larger near the surface than inside the multilayer. This is also reproduced by the model calculations of GISAXS pattern.

3. Brief theory

In DWBA approximation we should deal with the correct dependencies of the radiation field amplitudes inside multilayer for the incident (subscript $_i$) and scattered (subscript $_f$) waves in the forward ($^+$) and backward ($^-$) directions, calculated on the basis of the exact reflectivity theory for ideal structure. If z-axis is along the normal to the surface these amplitudes can be presented as

$$\begin{aligned} &E_i^+(z)\, e^{ik_i^\perp(z)z}\, e^{i\vec{k}_i^{\parallel}\vec{r}^{\parallel}},\ \ E_i^-(z)\, e^{-ik_i^\perp(z)z}\, e^{i\vec{k}_i^{\parallel}\vec{r}^{\parallel}},\\ &E_f^+(z)\, e^{ik_f^\perp(z)z}\, e^{i\vec{k}_f^{\parallel}\vec{r}^{\parallel}},\ \ E_f^-(z)\, e^{-ik_f^\perp(z)z}\, e^{i\vec{k}_f^{\parallel}\vec{r}^{\parallel}} \end{aligned} \tag{2}$$

respectively. The superscripts $\perp$ and $\parallel$ denotes the components of the wave vectors and radius vector perpendicular and parallel to the surface. The common factor $e^{-i\omega t}$ is omitted. Here we consider σ-polarization for all waves, and use scalar field amplitudes. Tangential components of the wave vectors $\vec{k}_i^{\parallel}$ and $\vec{k}_f^{\parallel}$ are unchanged with depth z. The normal components of the wave vectors have the following expressions [26]:

$$k_i^\perp(z) = \frac{2\pi}{\lambda}\sqrt{\sin^2(\theta_i) + \chi(z)},\ \ k_f^\perp(z) = \frac{2\pi}{\lambda}\sqrt{\sin^2(\theta_f) + \chi(z)}, \tag{3}$$

where $\chi(z)$ is the X-ray susceptibility for given wavelength (Susceptibility is simply connected with the often used refraction index n: if $n = \sqrt{\varepsilon} = 1 + \delta + i\beta$, then $\chi = 2\delta + 2i\beta$, δ is normally negative for X-ray wavelengths, β is positive in our complex space).

If the variations of the field amplitudes in volume V of the single particle is not essential, than the amplitude of scattering by this particle can be presented as [8]:

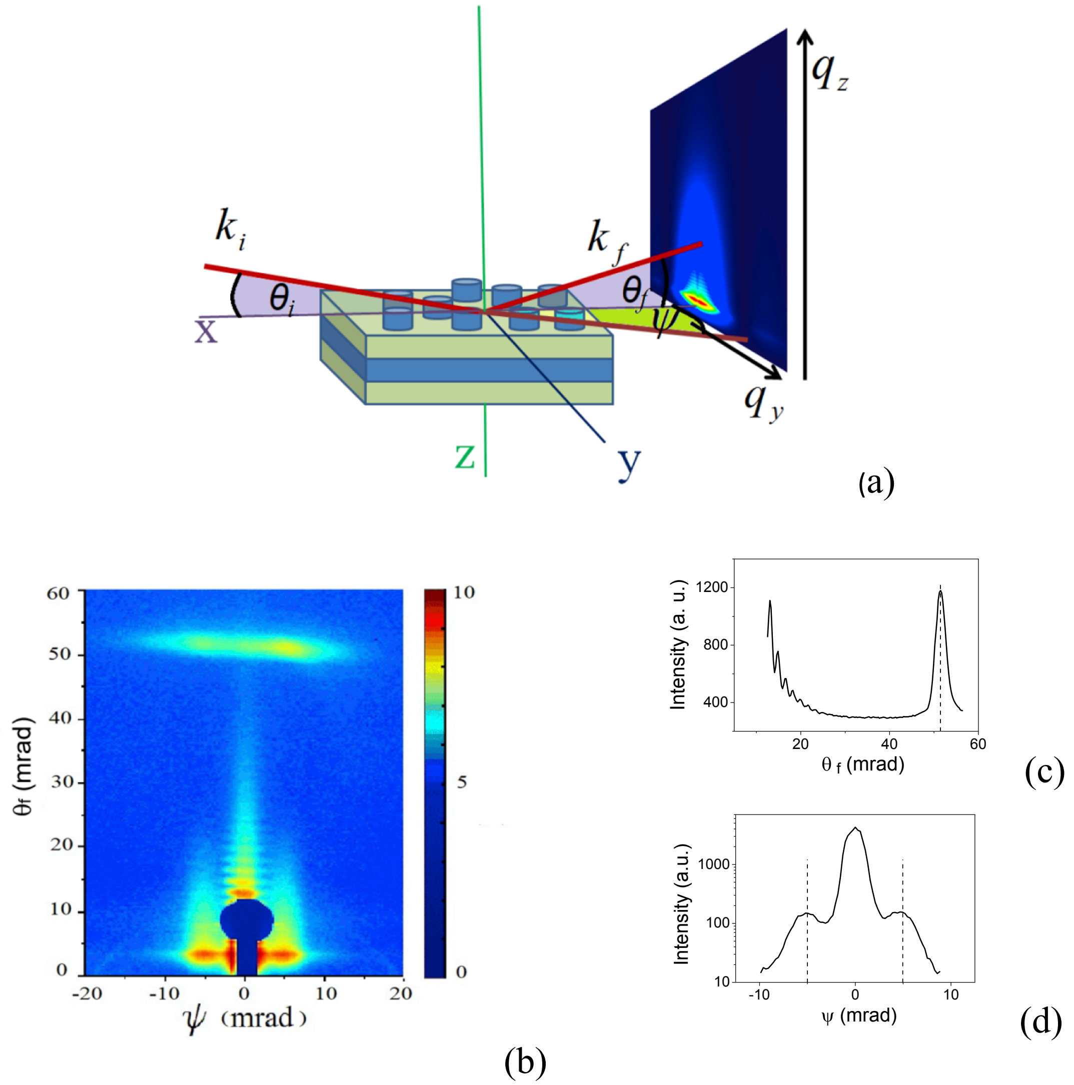

Fig. 1. (a) Scheme of the experiment, (b) GISAXS pattern measured for our sample and (c) its vertical near $\psi = 0$ and (d) horizontal near the critical angle cross sections.

$$\begin{aligned} &F(\vec{q}, z) = \\ &= E_i^+(z)E_f^+(z)F_{particle}(q^{\|}, q_{++}^{\perp}, z) + \\ &+ E_i^-(z)E_f^+(z)F_{particle}(q^{\|}, q_{-+}^{\perp}, z) + \\ &+ E_i^+(z)E_f^-(z)F_{particle}(q^{\|}q_{+-}^{\perp}, z) + \\ &+ E_i^-(z)E_f^-(z)F_{particle}(q^{\|}, q_{--}^{\perp}z)\,, \end{aligned} \tag{4}$$

where

$$F_{particle}(q^{\|}, q_{\pm\pm}^{\perp}, z) = \frac{1}{V}\int_V \Delta\rho(\vec{r})\exp(iq^{\|}\vec{r}^{\|})\exp(iq_{\pm\pm}^{\perp}z)\ d\vec{r}_{\|}dz, \tag{5}$$

$$q_{\pm\pm}^{\perp} = \pm k_f^{\perp}(z) \mp k_i^{\perp}(z), \tag{6}$$

$$q^{\|} = k_f^{\|} - k_i^{\|}, \tag{7}$$

and $\Delta\rho(\vec{r})$ is the deviation of the electron density in particle from the surrounding density. We can put $\Delta\rho(\vec{r}) = 1$ in the particle, and $\Delta\rho(\vec{r}) = 0$ in surrounding space. The absolute values of the scattering amplitudes can be taken into account in the final intensity expression.

For our sample with very small layer thicknesses it is clear that the variations of radiation fields along depth are very rapid so it is reasonable to apply the so called "slicing" for $F_{particle}$ calculation. Supposing in each thin m-slice $\Delta\rho(\vec{r})$ not depending on z, i.e. $\Delta\rho(\vec{r}) = \Delta\rho_m(\vec{r}^{\|})$ and $E^{\pm}_{i,f}(z)\, e^{\pm ik^{\perp}_{i,f}(z)z} = E^{\pm}_{i,f}(H_m/2)e^{\pm ik^{\perp}_{i,f}(z_m)\,\xi}$, where $E^{\pm}_{i,f}(H_m/2)$ is the value of the radiation field in the center of the slice and ξ changes in the limits $\pm\, H_m/2$, the integral over z in m-slice in (5) can be easily calculated. Taking into account the small thickness of the slice we get

$$\int_{-H_m/2}^{H_m/2} \exp(iq^{\perp}_{\pm\pm}\xi)\, d\xi = \frac{\exp(iq^{\perp}_{\pm\pm}H_m/2) - \exp(-iq^{\perp}_{\pm\pm}H_m/2)}{iq^{\perp}_{\pm\pm}} = \frac{2\sin(q^{\perp}_{\pm\pm}H_m/2)}{q^{\perp}_{\pm\pm}} \approx H_m\,. \tag{8}$$

So $F_{particle}$ in thin slices does not depend on $q^{\perp}_{\pm\pm}$. Therefore, the expression (4) for each m-slice is simplified to:

$$F_m(\vec{q}, z) = E^{tot}_i(z_m)E^{tot}_f(z_m)F_{particle}(q^{\|}, z_m)\,, \tag{9}$$

where

$$E^{tot}_{i,f}(z_m) = E^{+}_{i,f}(H_m/2) + E^{-}_{i,f}(H_m/2), \tag{10}$$

which is the total radiation field at depth z_m in m-slice. For its calculation the propagation matrices exist [26–28]:

$$\frac{d}{dz}\begin{pmatrix} E^{\sigma}(z) \\ H^{\sigma}_t(z)\end{pmatrix} = i\frac{\omega}{c}\hat{M}^{\sigma}(z)\begin{pmatrix} E^{\sigma}(z) \\ H^{\sigma}_t(z)\end{pmatrix}, \tag{11}$$

where $H^{\sigma}_t(z)$ is the tangential component of the magnetic field of radiation (proportional to the z-derivative of $E^{\sigma}(z)$) and the differential propagation matrix e.g. in the case of σ polarization has a form:

$$\hat{M}^{\sigma}(z) = \begin{pmatrix} 0 & 1 \\ \sin^2\theta + \chi(z) & 0 \end{pmatrix}. \tag{12}$$

For calculation of $F_{particle}(q^{\|}, z_m)$ we assume the simplest case of axial symmetry and get the well-known expression:

$$F_{particle}(q^{\|}, z_m) = \frac{H_m}{S}\int_S \Delta\rho_m(\vec{r}^{\|})\exp(i\vec{q}^{\|}\vec{r}^{\|})\; d\vec{r}^{\|} = 2\pi\,\Delta\rho_m\, H_m\, R_m^2\,\frac{J_1[q^{\|}R_m]}{q^{\|}R_m}, \tag{13}$$

where R_m is the radius of a cylinder (actually it is a thin disk with thickness of H_m). In computer calculations the following expression for Bessel function is used [29]:

$$J_1(x) = \frac{1}{\pi}\int_0^{\pi}\cos(\phi - x\sin(\phi))d\phi. \tag{14}$$

Taking in mind that the inhomogeneities in our sample are not artificial, the averaging over radius R_m has been applied and in addition some correlation in their arrangement in each m-slice has been used [8,23]:

$$\bar{F}_{particle}(q^{\|}, z_m) = 2\pi\,\Delta\rho_m\, H_m\,\sqrt{S(q^{\|})}\,\sum_n p_n R_n^2\frac{J_1[q^{\|}R_n]}{q^{\|}R_n}\Big/\sum_n p_n, \tag{15}$$

where $S(q^{\|})$ is a structure factor, d_{corr} is the nearest-neighbor distance and σ_d is its root-mean-square deviation. $S(q^{\|})$ has the following form in 1D paracrystal model [10,30,31]:

$$S(q^{\|}) = \frac{1 - \exp[-q^{\|}\sigma_d^2]}{1 + \exp[-q^{\|}\sigma_d^2] - 2\exp[-q^{\|}\sigma_d^2/2]\cos(q^{\|}d_{corr})}. \tag{16}$$

For uncorrelated inhomogeneities we put $S_m(q^{\|}) = 1$, this can take place in the interfaces and at this depth $\bar{F}_{particle}(q^{\|}, z_m)$ imitates the roughness contribution. For averaging among different sizes of inhomogeneities Gaussian function with width σ_m is used:

$$p_n = e^{-\frac{(R_n - R_m)^2}{2\,\sigma_m}}. \tag{17}$$

Finally, the coherent sum over all slices in the structure is performed and the total GISAXS intensity is calculated by the expression:

$$I(\vec{k}_i \to \vec{k}_f) \approx r_e\left|\sum_m E^{tot}_i(z_m)E^{tot}_f(z_m)\bar{F}_{particle}(q^{\|}, z_m)\sqrt{W_m}\right|^2 e^{-\sigma^{\perp 2}q^{\perp 2}}, \tag{18}$$

where

$$q^{\perp} = \frac{2\pi}{\lambda}(\sin\theta_i + \sin\theta_f). \tag{19}$$

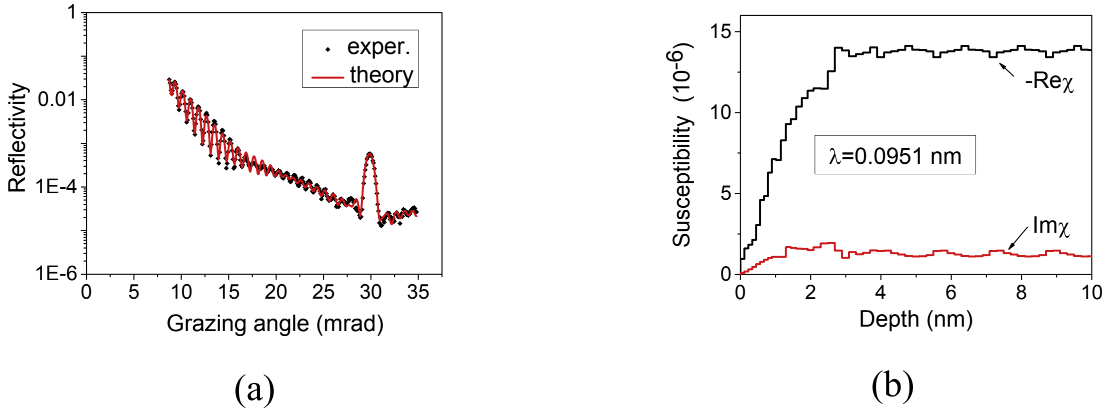

Fig. 2. (a) Normalized reflectivity at 0.0951 nm wavelength for the Al_2O_3/Cr(70 Å)/[^{57}Fe(8 Å)/Cr(10.5 Å)]$_{30}$/Cr(12 Å) sample (symbols are the experimental curve and solid line is the fit result) and (b) the obtained depth profiles of Reχ(z) and Imχ(z) (all 28 repetitions is not shown and only initial part of these functions is presented).

Factor $e^{-\sigma_{\perp}^2 q_{\perp}^2}$ (similar to the Debay-Waller factor) is included in order to take into account some lost of coherence in the interference of scattered waves from different slices with increasing angle. (More complicated formalism for the depth correlations of inhomogeneities is considered in Refs. [20,21,31]). Factor W_m is the relative "weight" of inhomogeneities in different slices, it depend on its relative electronic density (the absolute value of $\Delta\rho_m$ is more convenient to include to W_m) and density of inhomogeneity distribution.

4. Calculation of the GISAXS pattern

The modelling of the GISAXS pattern we have started from the fit of the X-ray reflectivity curve, measured for our sample at the same wavelength 0.0951 nm (Fig. 2(a)). Fit gives the period $D = 1.602$ nm and depth profiles of the real and imaginary parts of susceptibility, Re$\chi(z)$ and Im$\chi(z)$ respectively, drawn in Fig. 2(b). The program package REFSPC [32] has been used for the reflectivity fit. In this program the interface roughness is considered by the existence of the interfaces of variable thickness and error function profiles for Re$\chi(z)$ and Im$\chi(z)$ divided by some number of steps. The obtained depth profiles are rather complicated, the distortion of the top and bottom periods compared with the repetitive part is taken into account. The obtained values of Re$\chi(z)$ and Im$\chi(z)$ in Fe and Cr layers differ from the Table values [33] indicating their essential intermixing. Possible diffuse scattering results in the larger values of Im$\chi(z)$ obtained during the fit.

For the following usage of these profiles for GISAXS calculation the steps in depth profiles are adopted to the slicing for ~0.2 nm. In total we have ~50 slices and 8 of them are repeated 28 times. After that the additional fit to the experimental X-ray curve with these new steps has been done. The final procedure with reflectivity task is the calculation of the amplitude of the total radiation field $E(z)$ as a function of the grazing incidence (or exit) angles $\theta_{i,f}$, which is needed for calculation by formula (18). Squared module of this function is presented in Fig. 3.

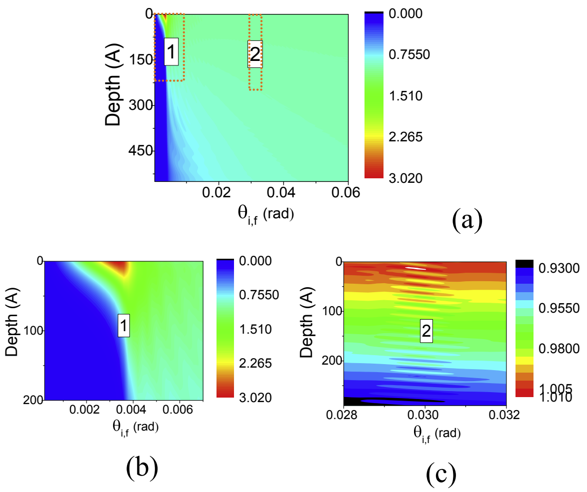

Fig. 3. (a) $|E_{i,f}^{tot}(z, \theta_{i,f})|^2$, calculated for the obtained Reχ(z) and Imχ(z) by the reflectivity curve fit; (b) and (c) the same in the selected angular regions near the critical angle and near the Bragg maximum.

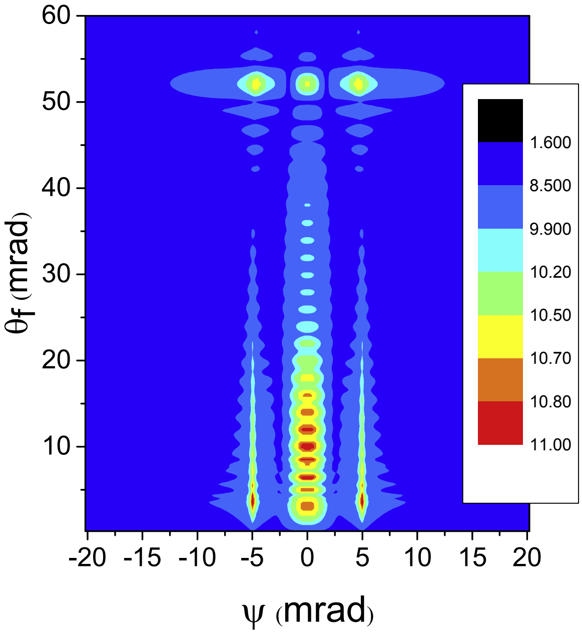

Fig. 4. Calculated GISAXS pattern (about the used parameters see text).

For calculation of GISAXS pattern the additional parameters should be defined for each slice, namely the relative weight of scattering amplitude W_m by inhomogeneities, the average radius of the disk R_m and width of their Gaussian distribution σ_m, the nearest-neighbor distance d_{corr} of inhomogeneities and its root-mean-square deviation σ_d:

At the moment we are not able to fit so huge amount of parameters (5 × 50 slices), so just qualitative similarity of the calculated GISAXS pattern is achieved (Fig. 4) by the handle variation of basic parameters.

The following description of the structure has been obtained. The top layer (~2.5 nm) is characterized by uncorrelated inhomogeneities with average size (some analog of the correlation length) of 18 nm and its distribution of ~8 nm. Then correlated granules exist with average radius of 5.5 nm, width of their Gaussian distribution of 1.5 nm, average distance of ~19.1 nm and its root-mean-square deviation of ~2 nm. The relative scattering from this second layer (W_m) is ~ twice stronger than from the top layer. The main contribution to the GISAXS picture the periodic part gives. It consists from the partially correlated and uncorrelated contributions thirty times stronger than surface scattering. The uncorrelated scattering is originated from Fe/Cr and Cr/Fe interfaces with thickness of ~0.2 nm. For the correlated part we get the inhomogeneities with average lateral size of ~2.5 nm, 2.4 nm width of their Gaussian distribution and vertical size of 0.4 nm, they are distributed with the average distance of ~19.1 nm and its root-mean-square deviation of ~4 nm.

It is a pity that at the used experimental wavelength it is not possible to distinguish the cases when inhomogeneities exist in the Fe or in the Cr layers. If we change in calculations the position of inhomogeneities for a half of period, than no change of the calculated GISAXS pattern appears.

5. Test of the X-ray standing wave influence

Insensitivity of the calculated GISAXS pattern to the position of the inhomogeneities in one period follows from the very small contrast of the susceptibilities between Fe and Cr layers for the used wavelength (being even smaller due to the layer intermixing). At such contrast the Bragg reflectivity is very low and the radiation field inside the structure has a negligible variation on the scale of one period. For the higher contrast of susceptibilities between constituents in one period the radiation field formed at Bragg condition supplies the selectivity in interaction with the separate parts in one period. That can be used for determination of which layer in period contains inhomogeneities, i.e. which layer is not continuous (in the case of very thin layer). The similar approach (waveguide effect) has been used for the enhancement of the scattering from nanostructures in thin film [23] and selective study of the interface roughness [34].

The higher contrast of susceptibilities between Fe and Cr takes place near the absorption edges. For instance, the variation of Fe susceptibility in vicinity of the $L_{2,3}$ edges is drawn in Fig. 5.

If we choose $\lambda = 1.7566$ nm then the contrast of susceptibilities in Fe and Cr layers is high enough:

$$\chi_{Fe} = (117.35 + 67.70\ i)\cdot 10^{-4}\ \ and\ \ \chi_{Cr} = (-35.35 + 31.87\ i)\cdot 10^{-4}\,. \tag{20}$$

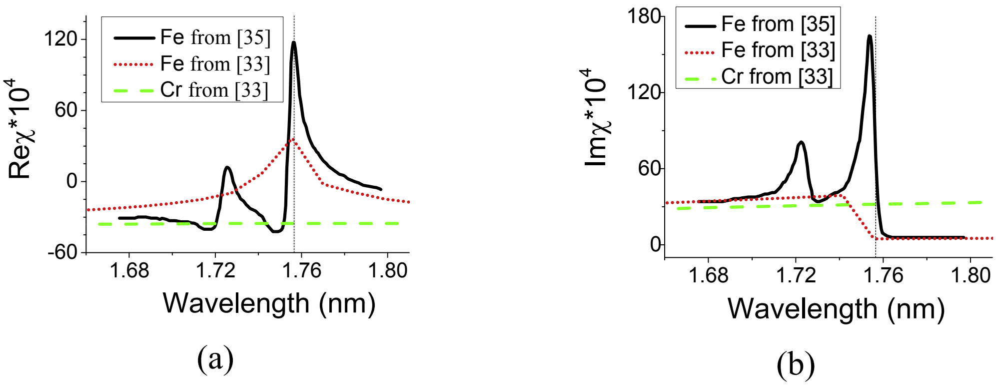

Fig. 5. Table values and experimentally obtained by XMCD measurements for Reχ (a) and Imχ (b) from Refs. [33], [35]. The dot vertical line denotes the chosen wavelength for model calculations.

At this wavelength the standing waves in our structure at Bragg condition should be rather good. The calculations for Figs. 6 and 7 are done for the same structure Al_2O_3/Cr(70 Å)/[^{57}Fe(8 Å)/Cr(10.5 Å)]$_{30}$/Cr(12 Å) with nominal parameters but for wavelength $\lambda = 1.7566$ nm and susceptibilities (20).

For demonstrating the depth selectivity on the scale of one period the angular dependencies of the fluorescence yield from Fe and Cr layers are calculated. The essential shift of the maximum on these dependencies is explained by the different position of the antinodes of the standing waves at different glancing angles. Basing on the fluorescence yield curves we can choose the incident angles as $\theta_i =$ 28.59°, 28.992° and 29.335° for calculating GISAXS patterns in order to enhance the scattering signal from inhomogeneities in Fe or Cr layers. The pictures in Figs. 8 and 9 are calculated with the following parameters of inhomogeneities: the lateral size is given as $R_m = 10$ nm, and for Fig. 9 the nearest-neighbor distance is defined as $d_{corr} = 67$ nm with its root-mean-square deviation $\sigma_d = 10$ nm.

In the θ_f dependencies of the scattering the angular shift between cases when inhomogeneities are situated in Fe or in Cr layers is clearly seen. This proves the principal possibility to distinguish the discontinuity of different layers in periodic multilayer by GISAXS method on conditions that the relevant parameters of the experiment will be provided.

6. Conclusions

In summary, we have presented the GISAXS image for the [Fe/Cr]$_{30}$ multilayer with ultrathin Fe and Cr layers measured at 0.0951 nm wavelength which has shown the Bragg peak, originated from periodic structure of inhomogineities, and side maxima for the exit angles near the critical angle and Bragg sheets, revealing the partial lateral correlation of the inhomogeneity distribution. The presented simplified GISAXS theory based on the DWBA approximation and thin slicing of the whole multilayer, allows of reproducing the basic features of the experimental pattern by proper depth distribution of the inhomogeneities. In order to show the possibility to use the x-ray standing waves for distinguishing the inhomogineity locations, the model calculations have been done as well for the wavelength in vicinity of the Fe L_3 edge, where the optical contrast between Fe and Cr layers is large enough to create noticeable X-ray standing waves. The results show the difference in the GISAXS pictures for the cases, when inhomogineities are placed in the Fe or in the Cr layers. In conclusion, we have demonstrated that the GISAXS method has a great potential for

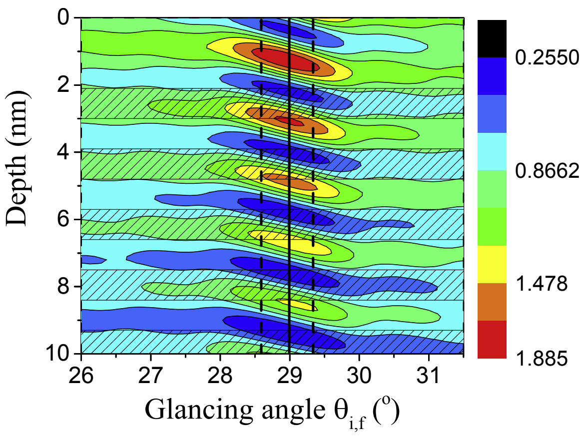

Fig. 6. $|E_{i,f}^{tot}(z, \theta_{i,f})|^2$ in vicinity of the Bragg peak calculated for $\lambda = 1.7566$ nm. The shaded regions represent positions of Fe layers.

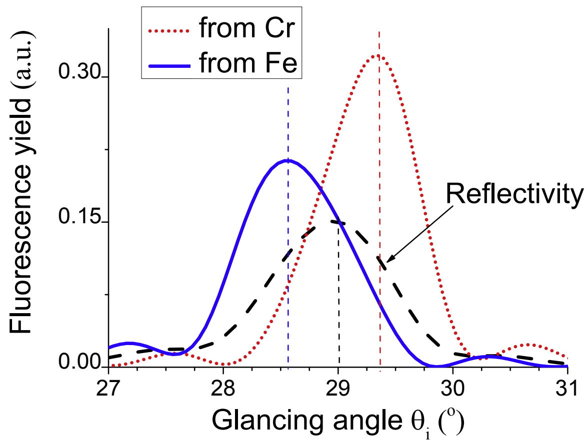

Fig. 7. Fluorescence yield from Fe and Cr layers as a function of the glancing angle for the incident radiation in vicinity of the Bragg peak.

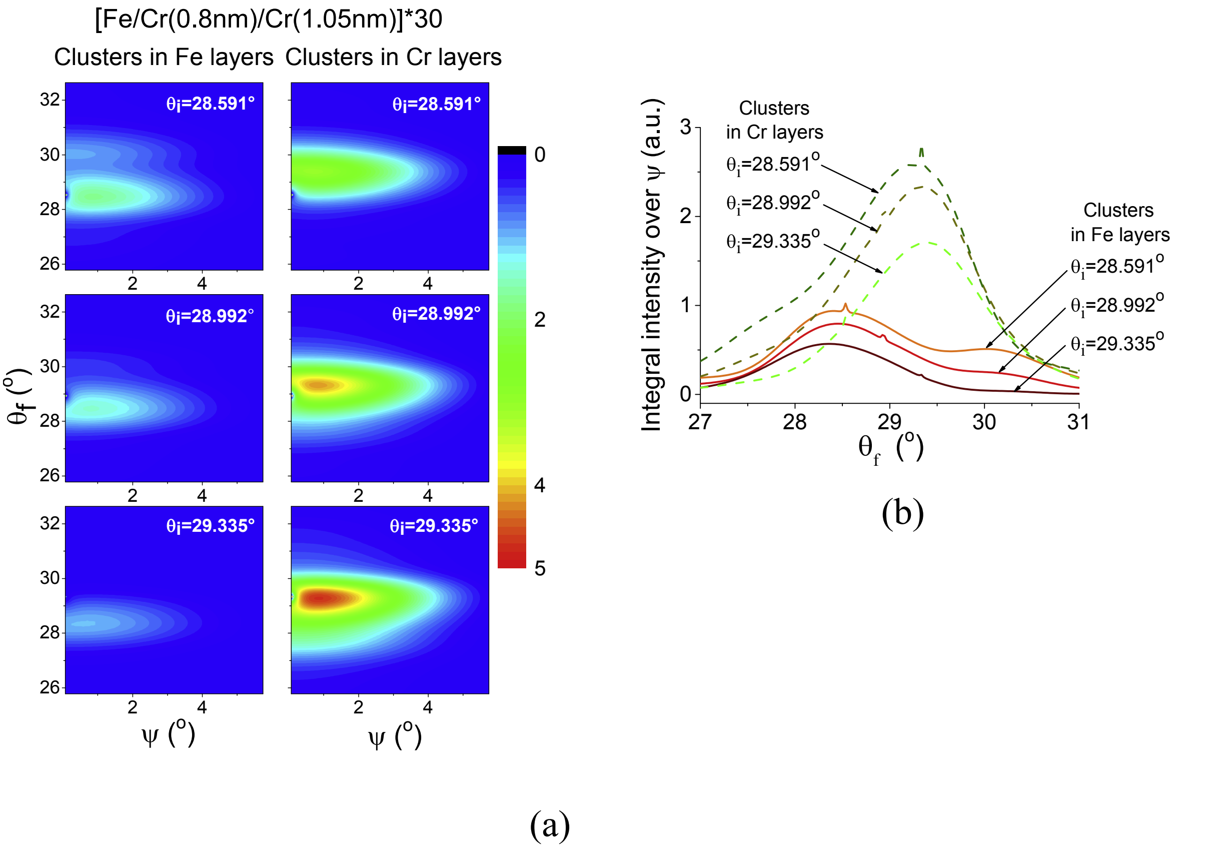

Fig. 8. **(a)** GISAXS pattern (right half) in vicinity of the Bragg peak for incident angles $\theta_i = 28.59°$, $28.992°$ and $29.335°$ in the case of the uncorrelated inhomogineities in Fe layers (left side) and in Cr layers (right side) and **(b)** their integrated horizontal cross sections as a function of the exit angle θ_f.

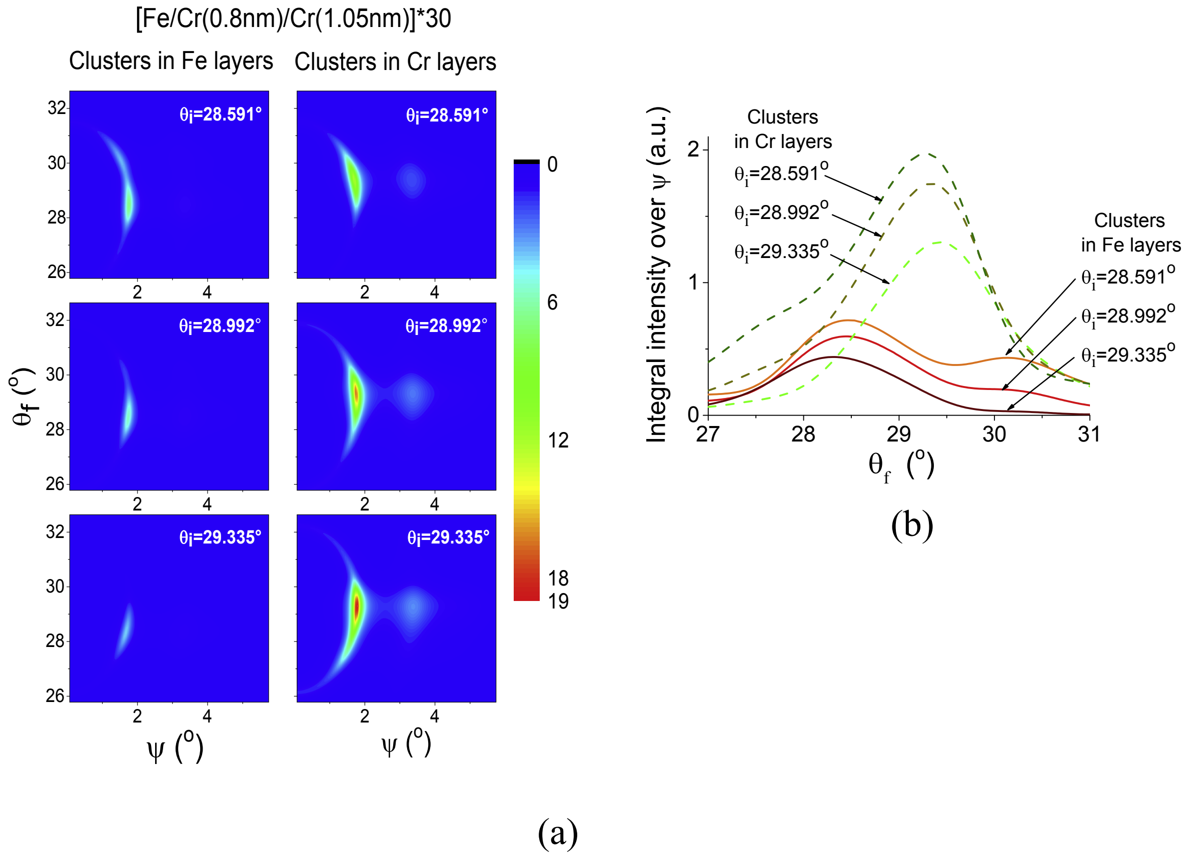

Fig. 9. **(a)** GISAXS pattern (right half) in vicinity of the Bragg peak for incident angles $\theta_i = 28.59°$, 28.992° and 29.335° in the case of the correlated inhomogineities in Fe layers (left side) and in Cr layers (right side) and **(b)** their integrated horizontal cross sections as a function of the exit angle θ_f.

characterizing a real structure of periodic multilayers and for detecting the discontinuity of definite layers.

Acknowledgements

The support by the Russian Foundation for Basic Research (Project Nos. 15-02-01502-a, 15-02-01674-a and 16-02-00887-a) is acknowledged. The authors thank Prof. Yu.A. Babanov, Dr. M.A. Milyaev and PhD. D.A. Ponomarev for the sample preparation. A.V.R. acknowledges a personal grant from the Foundation for the Advancement of Theoretical Physics and Mathematics “BASIS”. The GISAXS measurements were performed at the unique scientific facility Kurchatov Synchrotron Radiation Source supported by the Ministry of Education and Science of the Russian Federation (project code RFMEFI61917X0007).

References

[1] M. Wuttig, X. Liu, Ultrathin Metal Films, Magnetic and Structural Properties, Springer-Verlag Berlin Heidelberg, 2004.
[2] J.A.C. Bland, B. Heinrich (Eds.), Ultrathin Magnetic Structures III: Fundamentals of Nanomagnetism, Springer-Verlag Berlin Heidelberg, 2005.
[3] B. Drovosekov, N.M. Kreines, D.I. Kholin, A.V. Korolev, M.A. Milayev, L.N. Romashev, V.V. Ustinov, Spin-glass state of Fe/Cr multilayer structures with ultrathin iron layers, JETP Lett. (Engl. Transl.) 88 (2008) 118–122.
[4] V.V. Ustinov, L.N. Romashev, M.A. Milyaev, A.M. Burkhanov, Kondo-like effect in the resistivity of superparamagnetic cluster-layered Fe/Cr nanostructures, J. Magn. Magn Mater. 300 (1) (2006) 148–152.
[5] M.A. Andreeva, R.A. Baulin, A.I. Chumakov, R. Rüffer, G.V. Smirnov, Yu A. Babanov, D.I. Devyaterikov, M.A. Milyaev, D.A. Ponomarev, L.N. Romashev, V.V. Ustinov, Nuclear resonance reflectivity from $[^{57}Fe/Cr]_{30}$ multilayer with the Synchrotron Mössbauer Source, J. Synchrotron Radiat. 25 (2018) 473–483.
[6] M. A. Andreeva, R. A. Baulin, A. I. Chumakov, T. Yu Kiseleva, R. Rüffer, Polarimetry in Mossbauer Spectroscopy with Synchrotron Mossbauer Source, arXiv:1803.10117.
[7] G. Renaud, R. Lazzari, F. Leroy, Probing surface and interface morphology with grazing incidence small angle X-ray scattering, Surf. Sci. Rep. 64 (2009) 255–380.
[8] R. Lazzari, IsGISAXS: a program for grazing-incidence small-angle X-ray scattering analysis of supported islands”, J. Appl. Crystallogr. 35 (2002) 406–421.
[9] J.R. Levine, J.B. Cohen, Y.W. Chung, Thin film island growth kinetics: a grazing incidence small angle X-ray scattering study of gold on glass, Surf. Sci. 248 (1991) 215.
[10] G. Vignaud, A. Gibaud, J. Wang, S.K. Sinha, J. Daillant, G. Grübeland, Y. Gallot, An X-ray scattering study of laterally modulated structures: the example of diblock copolymers, J. Phys. Condens. Matter 9 (1997) L125–L130.
[11] A. Naudon, D. Babonneau, D. Thiaudiere, S. Lequien, Grazing-incidence small-angle X-ray scattering applied to the characterization of aggregates in surface regions, Physica B 283 (2000) 69.

[12] D. Babonneau, I.R. Videnović, M.G. Garnier, P. Oelhafen, Morphology and size distribution of gold nanoclusters in a − C:H films studied by grazing incidence small-angle x-ray scattering, Phys. Rev. B 63 (2001) 195401.
[13] D.-M. Smilgies, P. Busch, Ch M. Papadakis, D. Posselt, Characterization of polymer thin films with small-angle X-ray scattering under grazing incidence (GISAXS), Synchrotron Radiat. News 15 (2002) 35–42.
[14] P. Müller-Buschbaum, Grazing incidence small-angle X-ray scattering: an advanced scattering technique for the investigation of nanostructured polymer films, Anal. Bioanal. Chem. 376 (2003) 3–10.
[15] M. Schwartzkopf, A. Buffet, V. Korstgens, E. Metwalli, K. Schlage, G. Benecke, J. Perlich, M. Rawolle, A. Rothkirch, B. Heidmann, G. Herzog, P. Muller-Buschbaum, R. Rohlsberger, R. Gehrke, N. Stribeck, S.V. Roth, From atoms to layers: in situ gold cluster growth kinetics during sputter deposition, Nanoscale 5 (2013) 5053.
[16] D.J. Erb, K. Schlage, R. Röhlsberger, Uniform metal nanostructures with long-range order via three-step hierarchical self-assembly, Science Advances 1 (2015) e1500751.
[17] D. Babonneau, S. Peripolli, M.-F. Beaufort, J.-F. Barbot, J.-P. Simon, GISAXS study of cavities and {113} defects induced by neon and helium implantation in silicon, J. Appl. Crystallogr. 40 (2007) s350–s354.
[18] Z. Jiang, D.R. Lee, S. Narayanan, J. Wang, S.K. Sinha, Waveguide-enhanced grazing-incidence small-angle x-ray scattering of buried nanostructures in thin films, Phys. Rev. B 84 (2011) 075440.
[19] D. Erb, K. Schlage, L. Bocklage, R. Hübner, D.G. Merkel, R. Rüffer, H.-Ch Wille, R. Röhlsberger, Disentangling magnetic order on nanostructured surfaces, Phys. Rev. Materials 1 (2017) 023001(R).
[20] D. Babonneau, F. Petroff, J.-L. Maurice, F. Fettar, A. Vaurès, A. Naudon, Evidence for a self-organized growth in granular CoÕAl2O3 multilayers, Appl. Phys. Lett. 76 (2000) 2892–2894.
[21] P. Siffalovic, E. Majkova, L. Chitu, M. Jergel, S. Luby, J. Keckes, G. Maier, A. Timmann, S.V. Roth, T. Tsuru, T. Harada, M. Yamamoto, U. Heinzmann, Characterization of Mo/Si soft X-ray multilayer mirrors by grazing-incidence small-angle X-ray scattering, Vacuum 84 (2010) 19–25.
[22] H. Li, J. Zhu, Zh Wang, H. Chen, Yu Wang, J. Wang, Integration method for directly analyzing interface statistics of periodic multilayers from X-ray scattering, Phys. Rev. B 84 (2011) 075440.
[23] M. Buljan, N. Radić, S. Bernstorff, G. Dražić, I. Bogdanović-Radović, V. Holŷ, Grazing-incidence small-angle X-ray scattering: application to the study of quantum dot lattices, Acta Crystallogr. A68 (2012) 124–138.
[24] D. Altamura, V. Holý, D. Siliqi, I. Ch Lekshmi, C. Nobile, G. Maruccio, P.D. Cozzoli, L. Fan, F. Gozzo, C. Giannini, Exploiting GISAXS for the study of a 3D ordered superlattice of self-assembled colloidal iron oxide nanocrystals, Cryst. Growth Des. 12 (2012) 5505–5512.
[25] G. Benecke, W. Wagermaier, C. Li, M. Schwartzkopf, G. Flucke, R. Hoerth, I. Zizak, M. Burghammer, E. Metwalli, P. Müller-Buschbaum, M. Trebbin, S. Förster, O. Paris, S.V. Roth, P. Fratzl, A customizable software for fast reduction and analysis of large X-ray scattering data sets: applications of the new DPDAK package to small angle X-ray scattering and grazing-incidence small angle X-ray scattering, J. Appl. Crystallogr. 47 (2014) 1797–1803.
[26] M. Born, E. Wolf, Principles of Optics, Pergamon Press, 1968.
[27] G.N. Borzdov, L.M. Barkovskii, V.I. Lavrukovich, Zhurnal Prikladnoi Spectroskopii 25 (1976) 526 (In Russian).
[28] R. Azzam, N. Bashara, Ellipsometry and Polarized Light, North-Holland P.C., 1977.
[29] Angot, Compléments de mathématiques. A l'usage des ingénieurs de l'électronique et des télécommunications, Préface de Louis de Broglie, Paris, 1957 sec.7.5.11.
[30] B.K. Vainshtein, Diffraction of X-rays by Chain Molecules, Elsevier, Amsterdam, 1966 (Chap. V).
[31] F. Leroy, R. Lazzari, G. Renaud, Effects of near-neighbor correlations on the diffuse scattering from a one-dimensional paracrystal, Acta Crystallogr. A60 (2004) 565–581.
[32] http://www.esrf.eu/Instrumentation/software/data-analysis/OurSoftware/REFTIM-1.
[33] http://henke.lbl.gov/optical_constants/getdb2.html.
[34] D. Babonneau, S. Camelio, D. Lantiat, L. Simonot, A. Michel, Waveguiding and correlated roughness effects in layered nanocomposite thin films studied by grazing-incidence small-angle x-ray scattering, Phys. Rev. B 80 (2009) 155446.
[35] J.B. Kortright, S.-K. Kim, Resonant magneto-optical properties of Fe near its 2p levels: measurement and applications, Phys. Rev. B 62 (2000) 12216.